nature communications

Article

https://doi.org/10.1038/s41467-025-59662-w

Inorganic-organic hybrid metamaterials with switchable high stiffness and elasticity

Received: 4 June 2024

Accepted: 30 April 2025

Feihong Liu[1,6], Shasha Yao[2,3,6], Jia Li[1], Kejie Huang[1], Dongdong Zhang[1], Tak Man Wong[1,4], Ruikang Tang[5] ✉, Kelvin W. K. Yeung[1,4] ✉ & Jun Wu[1,4] ✉

In the pursuit of replicating the remarkable mechanical properties of natural biological composites like bone and seashell, developing artificial bulk materials that seamlessly integrate rigid inorganic components with ductile organic constituents has been a longstanding challenge. A key hurdle has been the establishment of robust and reliable linkages between these disparate building blocks. Mechanical metamaterials achieved by well-designed chemical structures, however, offer a promising solution to address this challenge. In this study, we demonstrate that the calcium phosphate-based inorganic-organic hybrid metamaterials trapping inorganic nanoparticles within long-chain polymeric networks and anchoring inorganic blocks to these networks via short-chain organic crosslinkers exhibit switchable and tunable high stiffness and elasticity. Additionally, these metamaterials not only exhibit peculiar mechanical characteristics, but also present excellent biocompatibility, as demonstrated by the in vivo tests using male rats and the in vitro tests. These results suggest a wide range of potential clinical applications.

Bulk materials historically face a dichotomy, boasting either a high stiffness or marked elasticity, rarely both concurrently. Illustrative of this, calcium phosphate-based (CaP) materials parallel the mechanical behavior of ceramics, revealing high yield strengths and an inherent stiffness, yet are compromised by brittle natures, a limitation impeding their broader application despite excellent biocompatibility and mechanical similarity to human osseous tissue[1,2]. The brittleness of CaP materials is owing to the rigid nature of their crystal structures, wherein microcracks propagate quickly under mechanical stress, resulting in sudden fracture[3]. In contrast, naturally occurring CaP-based biological materials, such as bones and seashells, achieve both robust stiffness and toughness through sophisticated inorganic-organic hierarchical structures at micro- and nanoscales[4]. Drawing inspiration from nature, researchers have sought to enhance the toughness of artificial bulk materials by integrating soft organic components and emulating biological structures[5,6].

There are two major challenges for developing inorganic-organic hybrid materials that amalgamate the constituent advantages; namely, establishing robust bonding between inorganic and organic constituents, and integrating their inherent mechanical properties without compromising their respective benefits. Commonly, the inclusion of ductile organic constituents to elevate material toughness paradoxically attenuates yield strength and stiffness. Concurrently, increased crosslinking degrees aiming to improve mechanical strength often result in diminished elasticity.

Breakthroughs in molecularly engineered organic-inorganic hybrids leveraging calcium carbonate oligomers and thioctic acid have heralded the simultaneous manifestation of ceramic, rubber, and

---

[1]Shenzhen Key Laboratory for Innovative Technology in Orthopaedic Trauma, Guangdong Engineering Technology Research Center for Orthopaedic Trauma Repair, Department of Orthopaedics and Traumatology, The University of Hong Kong-Shenzhen Hospital, Shenzhen, China. [2]Department of Orthopaedic Surgery, Sir Run Run Shaw Hospital School of Medicine, Zhejiang University, Hangzhou, Zhejiang, China. [3]Key Laboratory of Musculoskeletal System Degeneration and Regeneration, Translational Research of Zhejiang Province, Hangzhou, Zhejiang, China. [4]Department of Orthopaedics and Traumatology, School of Clinical Medicine, Li Ka Shing Faculty of Medicine, The University of Hong Kong, Hong Kong SAR, China. [5]Center for Biomaterials and Biopathways, Department of Chemistry, Zhejiang University, Hangzhou, Zhejiang, China. [6]These authors contributed equally: Feihong Liu, Shasha Yao.
✉e-mail: rtang@zju.edu.cn; wkkyeung@hku.hk; wuj7@hku-szh.org

plastic characteristics within a single material[7], evidencing the possibility of designing molecular structures that singularly harness the intrinsic virtues of inorganic and organic components. Mechanical metamaterials—principled on the attainment of extraordinary mechanical properties via strategic constituent arrangements[8,9]—may offer an alternative pathway towards materials that capitalize on these intrinsic virtues, yielding unprecedented features[10]. Until now, mechanical metamaterial endeavors predominantly focus on architectural manipulation, especially at the micro- and nanoscales[11], to evoke such unique properties as negative or zero Poisson's ratios[12,13], negative stiffness[14,15], and auxeticity[16,17]. To the best of our knowledge, bulk material with switchable high stiffness and elasticity has not been documented.

Previously, we have developed CaP nanoclusters with diameters of about 1 nm, which were formed and stabilized by crosslinking of Ca^{2+} with negatively charged long-chain polymers (polyacrylic acid, PAA; and poly-L-aspartic acid, PASP)[18]. This architectural blueprint constitutes a distinctive inorganic-organic chemical structure in which inorganic CaP nanoclusters are housed in organic long-chain polymer framework.

In this work, we introduce rigid inorganic segments into this framework, utilizing short-chain crosslinkers (citric acid, CA) to establish robust linkages between the rigid inorganic constituents and the CaP nanocluster junctions in ductile organic matrix. Herein, we detail the synthesis of a calcium phosphate-based inorganic-organic hybrid metamaterial (CIOHM) endowed with switchable high stiffness and elasticity. The metaproperty is achieved through the conception of a long-chain/short-chain dual inorganic-organic crosslinking network (L/SDIOCN) (Fig. 1A). Extensive characterizations of CIOHM ascertain the effectiveness of the L/SDIOCN strategy in pioneering mechanical metamaterials that seamlessly integrate the functional traits of both inorganic and organic constituents.

Results and discussion

Switchable stiffness and elasticity in CIOHM

Synthesized by reacting a solution phase—comprising calcium phosphate (CaP) nanoclusters with incorporated citric acid (CA)—with a powder phase composed of tetracalcium phosphate (TTCP) and dibasic calcium (DCPA), CIOHM solidifies over a period ranging from several minutes to tens of minutes. Pre-solidification, the material's malleable, paste-like state facilitates facile shaping (Fig. 1B, upper panel). The ensuing material can transition between two distinct states, as depicted in Fig. 1B (middle and lower panels). The initial ground state of CIOHM manifests pronounced stiffness, whereas, upon water uptake, it transforms into a hydration state characterized by increased volume and observable elastic deformation under compressive forces (Supplementary Figs. 1 and 2 and Supplementary Movies 1 and 2).

A thorough examination of the mechanical attributes of CIOHM, contrasted with calcium phosphate cements (CPCs), reveals distinct characteristics in both states, with uniaxial compression testing providing detailed insights (Fig. 1C). Despite hydration, the mechanical properties of CPC remain unaltered, as indicated by their consistent stress-strain profiles, with both hydrated and non-hydrated CPC samples exhibiting brittle fracture behavior and strains below the 5% threshold. In stark contrast, the ground state CIOHM (CIOHM-GS) displays a stress-strain response characteristic of plastic deformation, comprising three sequential phases: an initial rapid stress increase due to the incompressible nature of the CaP blocks, followed by a prominent deformation phase resulting from the reconfiguration of the polymeric networks, culminating in a secondary stress escalation as the CaP blocks densify under continued strain. This behavior underscores the amalgamation of CaP blocks' rigidity with the resilience of the polymeric networks within CIOHM, exhibited by its considerable fracture stress and deformation capacity.

When in the hydration state (CIOHM-HS), the material exhibits a starkly different, biphasic stress-strain profile: an initial phase entailed considerable strain with minimal associated stress, indicating water-induced swelling and subsequent elasticity of the polymer networks amid the more rigid CaP blocks. Even as the polymer networks dominate the material's mechanical response, the CaP blocks remain robustly tethered by CA, resulting in a second phase where compressive stresses rapidly mount with the decrease in distance between the CaP blocks. Such adaptable mechanical behaviors point to CIOHM as an emergent class of mechanical metamaterials.

Tensile properties are likewise appraised, corroborating the distinct mechanical personas presented by CIOHM in its respective states (Fig. 1D). While the elongations at break for both CPC and its hydrated counterpart are unremarkable, CIOHM-HS undergo substantial elongation at break, amounting to 19.3 ± 1.9%, surpassing that of CIOHM-GS, which stands at 4.9 ± 1.6%. This divergence further attests to the unique and contrasting mechanical behaviors of CIOHM. Notably, CIOHM demonstrates enhanced toughness and durability compared to traditional CaP materials, with CIOHM-GS showcasing a noteworthy toughness of 5.188 ± 0.721 MJ/m^3, outstripping the CPC measurement by more than an order of magnitude, as indicated in Fig. 1E. This toggling capability between CIOHM-GS and CIOHM-HS is proved to be reproducible, retaining its mechanical integrity and structural geometry after ten hydration-dehydration cycles, even after immersion in phosphate-buffered saline (PBS) for 70 days (Fig. 1F and Supplementary Fig. 2). Upon immersion in water, CIOHM transitions from its ground state to its hydration state in approximately 40 min (Supplementary Fig. 3A and B). Unsaturated CIOHMs are collected at intervals of 5, 10, 20, and 40 min for compressive and tensile tests. The results indicate that the hydration saturation level has no significant effect on stress-strain curves of CIOHM-HS (Supplementary Fig. 3C, E). Moreover, no significant differences are found in the tensile and compressive Young's moduli between saturated and unsaturated CIOHM-HS (Supplementary Fig. 3D, F).

Adjustable metaproperties and fatigue resistance of CIOHM

The emergent properties of CIOHM, with adjustable proportions of CA, are pivotal in defining its functionality. To delineate the roles of CA in CIOHM structure and performance, we evaluated CIOHMs containing varying CA contents—0.6 wt% and 1.2 wt%, respectively—and observed their influence on the metamaterial's formation. The solidification process can be characterized through rheological analysis immediately after combining the powder and solution phases. In the absence of CA, the rheological behavior indicates negligible storage (G′) and loss (G″) moduli of the mixture (below 50 Pa), pointing to an absence of cohesive inorganic-organic interactions (Fig. 2A). In contrast, with an incorporation of 0.6 wt% CA (0.6%CA-CIOHM), there is a significant elevation in G′ (red dots) to approximately 5 kPa and G″ (red squares) to around 2 kPa. The pronounced disparity between G′ and G″, where G′ greatly surpasses G″, suggests that the CIOHM is elastically dominant during the solidification stage[19]. Elevating the CA concentration to 1.2 wt% (1.2%CA-CIOHM) neither augments G′ (green dots) nor G″ (green squares), signifying a saturation point in CaP nanocluster crosslinking via CA.

The structural implications of CA presence within CIOHMs are also evident. CIOHMs containing CA are amenable to molding, whereas CA-absent CIOHMs exhibit pronounced shrinkage and cavity formation, attributable to disparate volume changes of the materials' inorganic and organic components and a lack of crosslinking during solidification. Moreover, CA-absent CIOHMs disintegrate upon water immersion and are unable to undergo a transition to a hydrated state (Supplementary Fig. 4). It is noteworthy, for the convenience of reference, that the non-metamorphic materials resulting from CA-absent solution phase reactions are still termed CA-absent CIOHM within this context. These findings underscore CA's integral role in

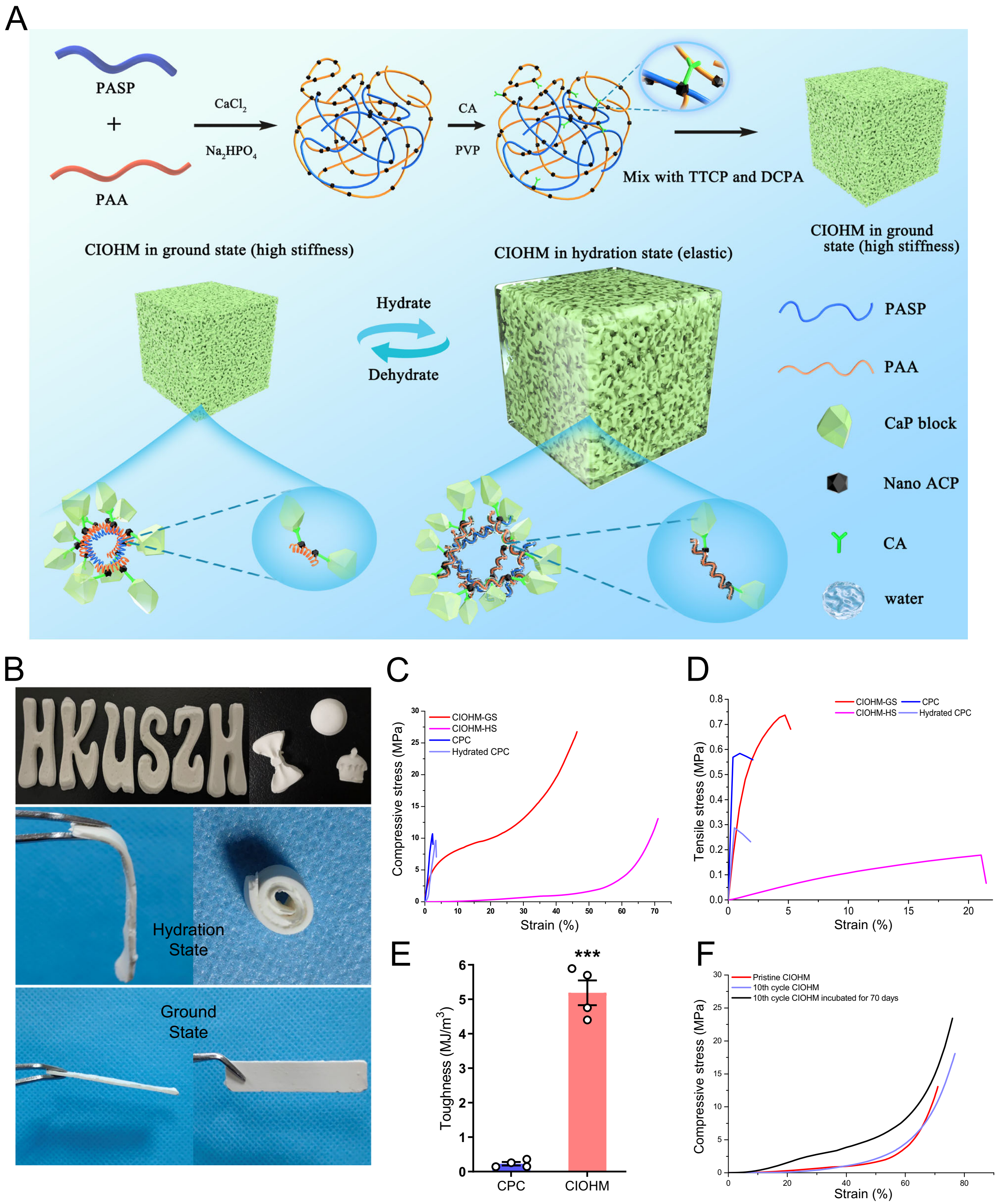

Fig. 1 | Mechanical behaviors of CIOHMs in ground and hydration states and their superior performance compared to traditional calcium phosphate cement (CPC). A Schematic representation detailing the synthesis of CIOHM and the underlying mechanism governing its transformation between ground and hydration states, which integrates the beneficial mechanical properties of rigid CaP blocks with ductile organic networks. **B** Sequential photographs illustrating the molding process of CIOHM: the initial shapeable material (top), the transformed elastic CIOHM in its hydration state (CIOHM-HS) (middle), and the hardened stiff CIOHM in its ground state (CIOHM-GS) (bottom). **C** Compressive stress–strain profiles comparing the mechanical response of traditional CPC and the CIOHM under compression. **D** Tensile stress–strain characteristics for both CPC and CIOHM, demonstrating the enhanced flexibility and strength of the CIOHM. **E** Comparison of the energy absorption capacity, quantified as toughness, between CPC and CIOHM, with CIOHM showing significantly higher toughness values. Data are presented as mean values +/− SEM ($n = 3$ biological replicates, ***: $P < 0.001$, *P*-Value = 0.0007, as determined by unpaired two-tailed Student's *t* tests). **F** Compressive stress–strain curves of CIOHMs in its hydration state (CIOHM-HS), evidencing the material's durability through 10 successive hydration-dehydration cycles without significant loss of mechanical performance. Such ability was maintained even after 70 days of incubation in phosphate-buffered saline (PBS) at 37 °C.

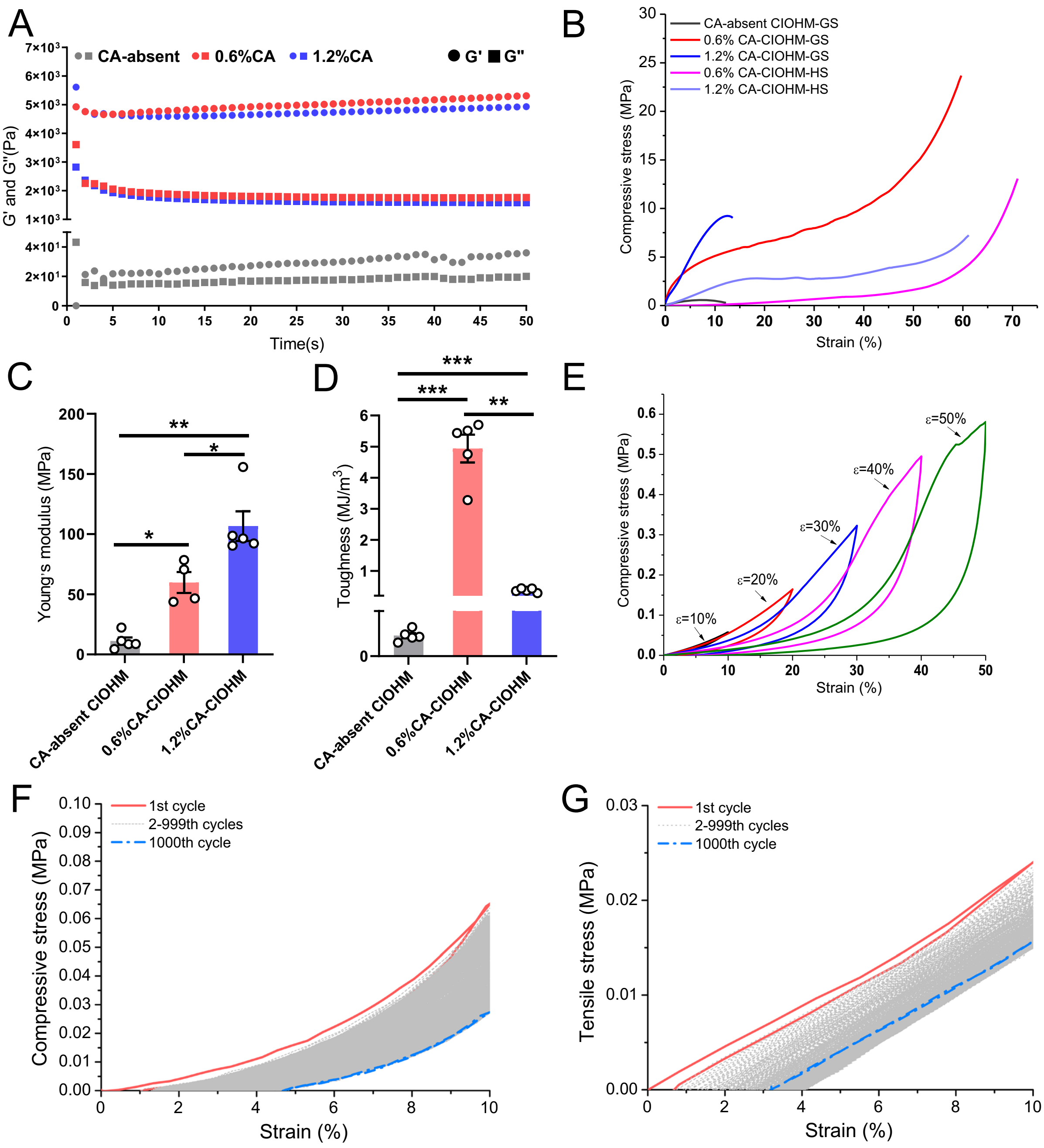

Fig. 2 | The role of citric acid (CA) content in modulating the setting process and mechanical properties of CIOHM. A Rheological analysis during the CIOHM setting phase, displaying the evolution of storage modulus (G′) and loss modulus (G″) over time, measured at a consistent oscillation frequency of 1 Hz. **B** Differential stress−strain response of CIOHM under varying concentrations of CA (absent, 0.6%, and 1.2% wt%) in both ground and hydration states, demonstrating CA's influence on material performance. **C** Variation of Young's modulus in the ground state of CIOHM associated with incremental CA content. *n* = 4 or 5 biological replicates, *: *P* < 0.05, **: *P* < 0.01, *P*-Value (CA-absent CIOHM vs. 0.6%CA-CIOHM) = 0.0156, *P*-Value (CA-absent CIOHM vs. 1.2%CA-CIOHM) = 0.0024, *P*-Value (0.6%CA-CIOHM vs. 1.2%CA-CIOHM) = 0.0419, one-way ANOVA with Games-Howell's post hoc test. **D** Toughness of CIOHM in the ground state with varying CA compositions, with the statistical significance of increases corresponding to higher CA concentrations. *n* = 5 biological replicates, **: *P* < 0.01, ***: *P* < 0.001, *P*-Value (CA-absent CIOHM vs. 0.6%CA-CIOHM) = 0.0009, *P*-Value (CA-absent CIOHM vs. 1.2%CA-CIOHM) = 0.0005, *P*-Value (0.6%CA-CIOHM vs. 1.2%CA-CIOHM) = 0.0011, one-way ANOVA with Games-Howell's post hoc test. **E** Elastic behavior under uniaxial compression of CIOHM in hydration state, examining deformation at controlled strain increments of 10, 20, 30, 40, and 50%. **F** Cyclic compression fatigue characterization at 1000 cycles for CIOHM in hydration state, assessing the endurance limits under repeated loading. **G** Cyclic tensile fatigue characterization at 1000 cycles for CIOHM in hydration state, illustrating the material's durability in tension. Data in C and D are presented as mean values +/− SEM.

binding inorganic CaP blocks with organic polymer networks, a necessity for the manifestation of metamaterial characteristics.

CA concentration also critically impacts the mechanical properties of the solidified CIOHMs. As demonstrated in Fig. 2B, the exclusion of CA produces a material with subpar yield strength, yet even nominal CA inclusion radically modified the profile of the compressive stress-strain curve and significantly enhanced mechanical robustness. Incrementing CA content from 0.6 wt% to 1.2 wt% leads to an increase in the Young's modulus of CIOHM in the ground state (Fig. 2C) at the expense of a reduction in toughness (Fig. 2D). Given that CA is a recognized calcium chelator[20–23], augmented CA levels not only promote inorganic-organic network linkages but also heightens the degree of crosslinking among the CaP blocks. Adjusting CA concentration thus permits the tuning of CIOHM's mechanical properties by balancing the ductile polymer network and rigid block contributions, enabling tailoring to specific application demands. Subsequent investigations focused on 0.6% CA-CIOHM, which displayed superior toughness.

In its hydrated state, CIOHM is characterized by notable elasticity and complete reversibility regarding its compressive response, sustaining up to 50% strain (Fig. 2E and Supplementary Movie 2). Furthermore, the mechanical durability of CIOHM when hydrated is remarkably stable; it withstands a thousand cycles of uniaxial compression or tension with less than a 5% strain in length deformation rates (Fig. 2F, G), with a few emergent deformities. As the number of cycles increase, the residual strain gradually rises until it reaches a constant value. This change is likely attributable to Mullins effect, a phenomenon commonly observed in rubber-like materials[24]. This further indicates that CIOHM-HS exhibits elastic features.

CIOHMs exhibit long-term mechanical stability

We further investigated the long-term mechanical stability of CIOHM by immersing samples in PBS and incubating them at 37 °C for 70 days. Compressive tests reveal no significant differences in the stress-strain curves and Young's moduli between pristine and incubated CIOHMs (Supplementary Fig. 5A, B). Notably, the toughness of incubated CIOHM is significantly higher than that of pristine CIOHM (Supplementary Fig. 5C). CIOHM also demonstrates the ability to withstand temperature changes ranging from 4 °C to 60 °C, covering the typical requirements for biomaterials. This is evidenced by the stress-strain curves and Young's moduli measured across different temperatures (Supplementary Fig. 5D, E). However, the toughness of CIOHM decreases at 60 °C, likely due to the weakening of hydrogen bonding (Supplementary Fig. 5F). Importantly, even after long-term incubation, CIOHMs retain their switchable mechanical features, including elastic properties in hydration state (Supplementary Fig. 5G), and demonstrate high fatigue resistance (Supplementary Fig. 5H).

Metaproperty in CIOHM is achieved by formation of L/SDIOCN

The unique mechanical properties of the CIOHM are attributed to the creation of a long-chain/short-chain dual inorganic-organic crosslinking network (L/SDIOCN). During the CIOHM preparation, in the solution phase, CA initially bonds with CaP nanoclusters, which are sequestered within polymeric networks, via carboxyl groups. Subsequent mixing with the powder phase results in CaP blocks, derived from the dissolution of DCPA and TTCP, binding to the remaining unreacted carboxyl groups of CA. These CaP blocks are thus anchored to the organic networks, forming the L/SDIOCN (Fig. 3A). This unique chemical architecture endows CIOHM with switchable mechanical states—high stiffness in the ground state due to the dominance of rigid inorganic CaP blocks and malleable toughness and plastic fracture characteristics underpinned by robust CA linkages between CaP blocks and the organic matrix. Upon hydration, the polymer network swells, expanding the spacing between CaP blocks, and temporarily conferring elasticity to the material, while still maintaining its inherent rigidity, allowing it to exhibit high mechanical strength when compressed.

The metaproperties are further elucidated through spectroscopic analyses, with attenuated total reflectance Fourier transform infrared (ATR-FTIR) spectra of CA-absent CIOHM, 0.6%CA-CIOHM, and 1.2%CA-CIOHM illustrating specific band patterns (Fig. 3B). Notably, intense bands at 558, 621, and 1051 cm^{-1} correspond to PO_4^{3-} within the calcium phosphate structure, while a pronounced peak at 3100–3500 cm^{-1} denotes the presence of hydrogen bonding. The latter is especially prominent in 1.2% CA-CIOHM, indicative of a higher degree of hydrogen bonding facilitated by the increased CA concentration. X-ray diffraction (XRD) profiles reveal that the crystalline phases present are similar to calcium phosphate cements (CPC), primarily consisting of alpha-tricalcium phosphate (α-TCP) and hydroxyapatite (HAP)[25] (Fig. 3C). X-ray photoelectron spectroscopy (XPS) further distinguishes the varied CA content within CIOHMs, with identifiable peaks for elemental constituents such as C *1s*, N *1s*, O *1s*, Ca *2p*, and P *2p* (Fig. 3D). The shift of Ca $2p_{1/2}$ and Ca $2p_{3/2}$ peaks[26] upon incorporating CA implies a reaction between Ca^{2+} and CA (Fig. 3E), while P *2p* peaks[27] remain unaffected (Fig. 3E).

Both ATR-FTIR and XRD data confirm the similarity in organic and inorganic components across the CIOHM varieties. Nevertheless, XPS results validate the CA-induced linkages in CA-containing CIOHMs, which are crucial for the observed enhancement in mechanical strength and the endowment of metaproperties. These results suggest that entrapping inorganic nanoparticles within polymeric networks as junctions, and subsequently bridging rigid inorganic elements to these junctions using short-chain crosslinkers to form L/SDIOCN, is a promising strategy to synthesize bulk mechanical metamaterials that fuse organic and inorganic features.

Transmission electron microscopy (TEM) images further visualize the distribution of CaP nanoclusters throughout the CIOHM matrix (Fig. 4A). High-resolution transmission electron microscopy (HRTEM) images reveal that small-sized CaP nanoclusters are uniformly dispersed throughout the 0.6% CA-CIOHM matrix, consistent with the TEM results. The corresponding elemental mapping analysis identifies the presence of C, O, N, Ca, and P elements within the 0.6% CA-CIOHM composites and further confirms the even distribution of the nanoclusters (Fig. 4B).

Scanning electron microscopy (SEM) illustrates that ground and hydrated states of CIOHM exhibit distinct microstructures, with noticeable porosity in the hydrated state owing to water uptake[28]. This suggests that the organic networks absorb water, thereby increasing porosity, which in turn elevates the water content of CIOHM-HS. (Fig. 4C). Energy-dispersive X-ray spectroscopy (EDS) mappings showed the elemental distribution in CIOHM-GS and CIOHM-HS (Fig. 4D). Thermogravimetric and differential thermal (TG/DTA) analyses reveal an exothermic peak between 250 and 400 °C associated with the decomposition of organic components (Fig. 4E). TG curves quantify the compositions of the CA-absent CIOHM, 0.6% CA-CIOHM and 1.2% CA-CIOHM, including water, organics, and mineral content, which align with the experimental formulation (Fig. 4F).

We investigated the long-term chemical stability of CIOHMs by incubating them in PBS at 37 °C. No significant weight loss was observed over 28 days (Supplementary Fig. 6A). ATR-FTIR (Supplementary Fig. 6B and C) and XRD (Supplementary Fig. 6D and E) spectra of CIOHMs collected at different time points post-incubation show no discernible chemical changes during this period. These results suggest that the L/SDIOCN can enhance the chemical stability of both inorganic and organic constituents.

Biocompatibility assessment of CIOHM

The investigation into the biocompatibility of the CIOHM yields promising results. Scanning electron microscopy (SEM) images provide visual confirmation that cells not only adhere to the CIOHM surface but also exhibit robust growth (Fig. 5A). Quantitative assessment via Cell Counting Kit-8 (CCK-8) assays corroborate these findings, revealing excellent biocompatibility in CIOHMs (Fig. 5B). The biocompatibilities of CIOHMs are evaluated using a Live/Dead assay and Cell Counting Kit 8 (CCK8) during 1, 3, and 5 days of culture. After co-incubation with extractions of CIOHMs for 1, 3, and 5 days, no significant differences are observed in the viabilities of hBMMSCs between the control and CIOHM groups (Fig. 5B). The Live/Dead assay results demonstrate the fusiform-like morphology of MSCs in both the control and CIOHM groups at each time point. Over the 5-day

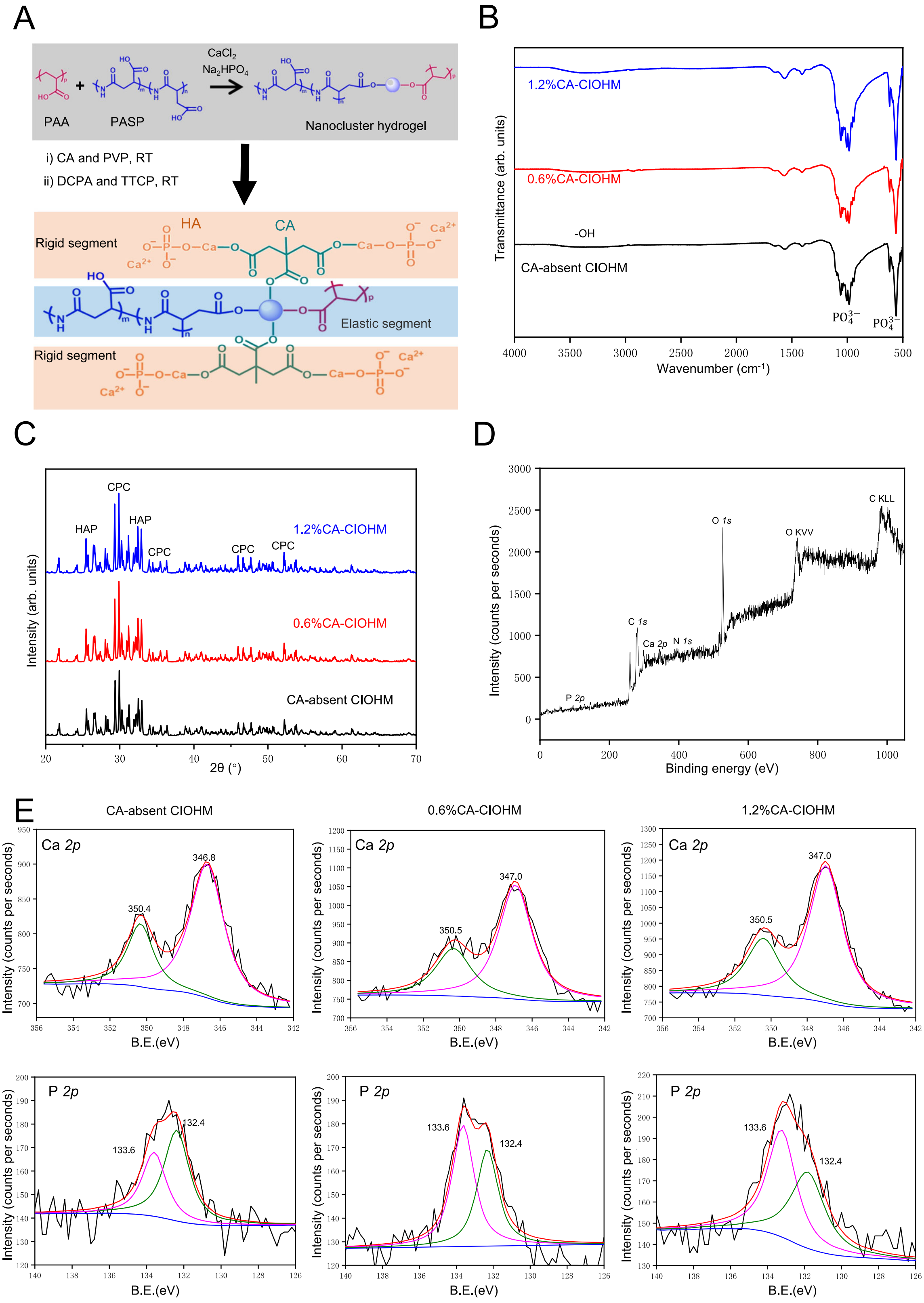

Fig. 3 | Chemical structure and compositional analysis of CIOHMs with varying CA levels. A Schematic representation of the CIOHM synthesis process, detailing the molecular architecture and emphasizing the role of CA as a crosslinking agent within the hybrid material. Gray area: synthesis of nanocluster hydrogel. Orange area: chemical structures of the rigid segment. Blue area: chemical structures of the elastic segment. **B** Attenuated total reflection Fourier-transform infrared (ATR-FTIR) spectra highlighting the chemical signatures of CIOHMs formulated with differing CA concentrations (absent, 0.6%, and 1.2%, wt%). **C** X-ray diffraction (XRD) patterns of CIOHMs, showing level of CA has no influence on the crystalline phases of CIOHM. **D** A survey X-ray photoelectron spectroscopy (XPS) spectrum of CIOHM, providing a broad overview of the elemental composition and chemical states present in the material. **E** High-resolution XPS spectra for Ca *2p* and P *2p* core levels in CIOHMs infused with varying proportions of CA (absent, 0.6%, and 1.2%, wt%), implying the reaction between CA and Ca. Blue lines were baselines. Green and purple lines were fitted curves of binding energies.

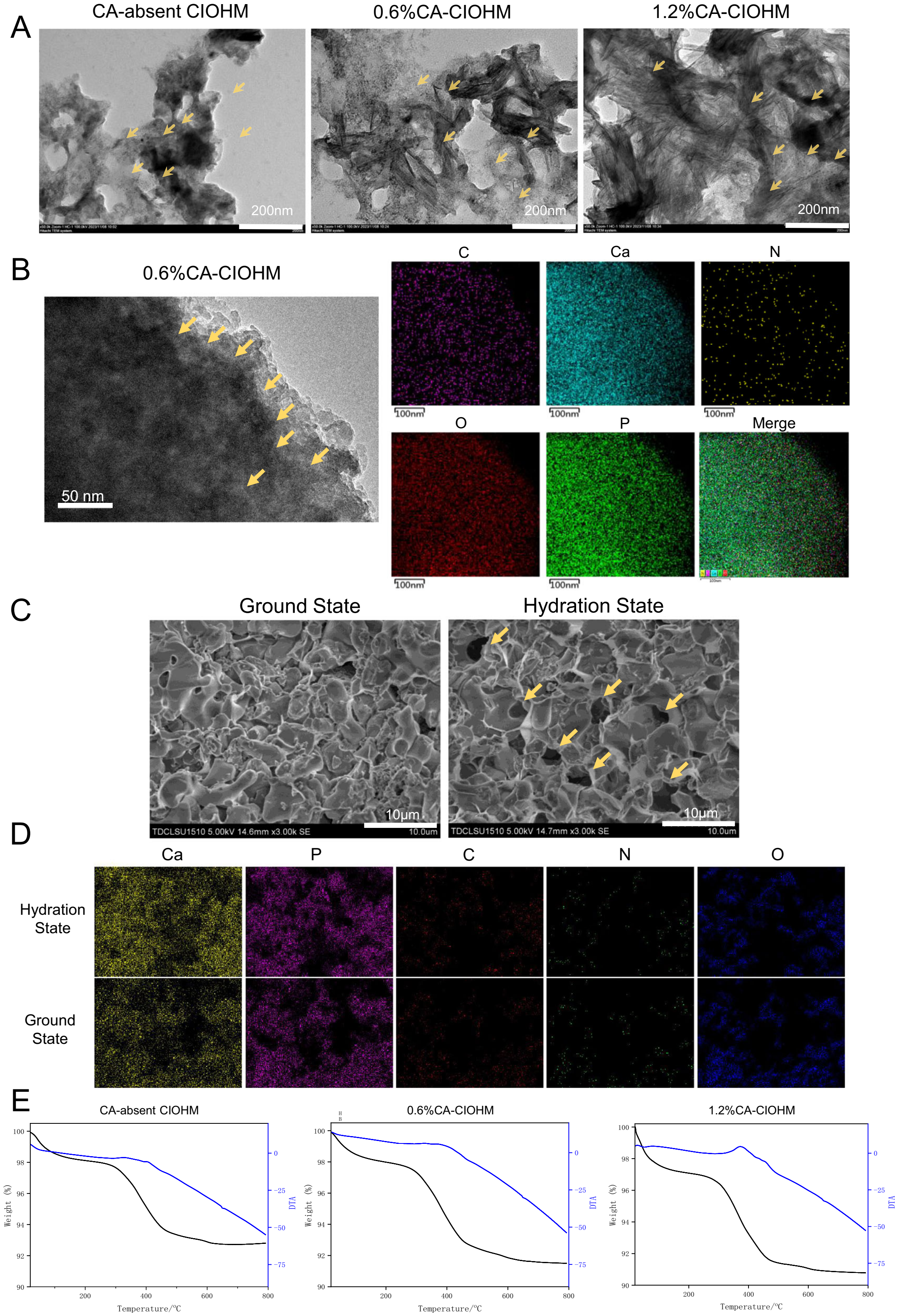

incubation period, the number of live cells in these groups increases significantly (Fig. 5C). Gene expression analyses of RAW264.7 cells on day 3 reveal no significant difference in *Il1b* levels between the CIOHM and control groups. *Tnfa* is down-regulated, while *Tgfb1* and *Il6* are up-regulated, with all fold changes less than 2 (Fig. 5D–G). These results indicate that CIOHM has mild effects on immune cells. The hemolytic potential of CIOHM, a critical consideration for implantable materials, is found to be minimal with an average hemolytic rate of 2.862 ± 0.06% (Fig. 5C), comfortably within the acceptable range for biomedical application (< 5%)[29]. Further coagulation assays afford insight into the material's interaction with the blood coagulation pathways. The extension in activated partial thromboplastin time (APTT; 35.51 ± 0.229 s) and thrombin time (TT; 36.22 ± 3.546 s) indicates a possible engagement with the intrinsic coagulation cascade and a

Fig. 4 | Microstructural and compositional analysis of CIOHMs with varying CA contents. A Transmission electron microscopy (TEM) images illustrating the internal microstructures of CIOHMs at various CA contents (absent, 0.6%, and 1.2%, wt%) (Independent experiments were repeated no less than three times). CaP nanoclusters are indicated by yellow arrows. Scale bar: 200 nm. **B** High-resolution transmission electron microscopy (HRTEM) images and Energy-dispersive X-ray spectroscopy (EDS) elemental mappings illustrating the internal microstructures of 0.6%CA-CIOHM (Independent experiments were repeated no less than three times). CaP nanoclusters are indicated by yellow arrows. Scale bar: 50 nm (HRTEM) and 100 nm (EDS). Purple dots: C element. Blue dots: Ca element. Yellow dots: N element. Red dots: O element. Green dots: P element. **C** Scanning electron microscopy (SEM) images showing the surface morphology of CIOHMs in both the ground and hydration states (Independent experiments were repeated no less than three times). The presence of pores formed during hydration is denoted by yellow arrows. Scale bar: 10 μm. **D** Energy-dispersive X-ray spectroscopy (EDS) elemental mapping of CIOHMs, illustrating the distribution of constituent elements in both the ground and hydration states. Yellow dots: Ca element. Purple dots: P element. Red dots: C element. Green dots: N element. Blue dots: O element. **E** Thermogravimetric (TG) alongside differential thermal analysis (DTA) curves for CIOHMs with different CA contents (absent, 0.6%, and 1.2%, wt%). The TG lines are represented in black, while the DTA results are indicated in blue.

moderate anticoagulant effect (Supplementary Fig. 7)[30,31]. It is imperative to note that neither prothrombin time (PT) nor the fibrinogen concentration (FIB) displayed any discernible alteration, suggesting that CIOHM's anticoagulant properties could be mild and localized.

We implanted CIOHM subcutaneously in rats to assess potential systemic acute and subacute toxicity. The complete blood count was performed at 24 h and 28 days post-implantation (Fig. 5H). However, due to the large standard error of the mean observed, statistical analysis may not reflect the authentic significance. Therefore, the biocompatibility of CIOHM was further investigated by clinical symptom observations and histopathological examinations. Throughout the experiment, no abnormal clinical symptoms are observed in any of the rats (Supplementary Table 2). By the study's endpoint, there are no differences in the weight or appearance of the liver, kidneys, and lungs between the two groups (Supplementary Fig. 8). Long-term in vivo studies in rats disclose no evidence of inflammatory response or pathological morphological changes in critical organs such as the lungs, liver, and kidneys post-implantation (Fig. 5I). These findings collectively indicate that CIOHM has minimal systemic impact, confirming its biocompatibility and potential for diverse clinical applications.

In vivo bone regeneration assessment of CIOHM

The CIOHM exhibits exceptional meta-properties, alongside high mechanical robustness and biocompatibility, positioning them as strategic materials for translational medicine. In particular, CaP-based materials have a longstanding history in the clinical domain, primarily serving as bone fillers for repairing deficits stemming from trauma, neoplastic activities, and other pathological bone losses[32–35].

Through a series of in-depth in vivo osteogenic assays and rat femoral condylar bone defect models, our data substantiate the regenerative capabilities of CIOHM (Fig. 6A–C and Supplementary Fig. 9). After implantation, CIOHM transitions into a flexible hydrated state, fostering cell infiltration and enhancing tissue integration at a nascent stage—a phenomenon lucidly depicted in our histological analyses (Fig. 6D). This biological interaction not only accelerates the regeneration process but also fortifies the union between the hybrid metamaterial and the native tissue.

Revolutionizing bone fracture management

Our research extends to innovate bone fracture treatment, advancing the concept of bone filling granules crafted from CIOHM, demonstrated in an animal model. The conventional approach to bone defect management involves bone cements, which rely on creating a viscous paste by mixing liquid and powder components—a process that is time-consuming.

CIOHM's potential becomes evident when considering the operational efficiency it can bring to the surgical arena. As a premade and sterilized granule, it can be readily applied to bone cavities during surgery, eliminating intergranular spaces upon transition into its expanded hydration state, underlined by our results (Fig. 6E and Supplementary Fig. 10). Thus, CIOHM exemplifies a significant advancement in orthopedic surgery techniques, potentially curtailing operation times.

Potential applications in reconstructive surgery

Our findings suggest broader clinical applications for CIOHM beyond orthopedic use. The properties it embodies make it amenable for utilization as a mandibular prosthesis in reconstructive surgery (Supplementary Fig. 11) and warrant further investigation into its application in diverse medical scenarios.

In this study, we successfully synthesized a calcium phosphate-based inorganic-organic hybrid metamaterial (CIOHM), whose distinguishing feature is its ability to switch between states of high stiffness and elasticity. This transformative capability arises from a unique long-chain/short-chain dual inorganic-organic crosslinking network (L/SDIOCN). Here, rigid CaP blocks are seamlessly integrated with flexible polymer networks through intermediate structures comprising citric acid and CaP nanoclusters embedded in polymer networks. This construction not only bestows the material with its remarkable metaproperties but also ensures robust mechanical integrity.

CIOHM opens a new chapter in the applications of metamaterials within the biomedical field. For instance, it offers a revolutionary strategy for the treatment of bone fractures. Unlike conventional bone cements, CIOHM can be pre-formed into sterilized granules, streamlining surgical procedures by negating the need for on-site mixing and curing, thereby facilitating a faster and potentially safer clinical practice. Furthermore, the long-term mechanical and chemical stability, combined with excellent plasticity during setting, warrant its application in implants, reconstructive surgeries, and a variety of other medical scenarios. More broadly, the successful creation of CIOHM exemplifies the vast potential of L/SDIOCN systems. This approach provides a versatile blueprint for engineering advanced bulk mechanical metamaterials that synergistically harness the desirable properties of both inorganic and organic components, setting a precedent for future material innovation.

Methods

Synthesis of the CIOHM

The CIOHM was fabricated through a reaction between a solution phase and a powder phase. The solution phase consisted of calcium phosphate (CaP) nanoclusters[18], with additions of citric acid and polyvinylpyrrolidone, was prepared as described below. Briefly, 0.1110 g of calcium chloride ($CaCl_2$, 97%, Sigma-Aldrich, USA, CAS No. 10043-52-4, eye irritation) was dissolved in 10 mL of deionized water to prepare a 0.1 M $CaCl_2$ solution. 0.1420 g of sodium phosphate dibasic (Na_2HPO_4, 99%, Sigma-Aldrich, USA, CAS No. 7558-79-4, not a hazardous substance or mixture) was dissolved in 10 mL of deionized water to obtain a 0.1 M Na_2HPO_4 solution. 3 g of poly (acrylic acid) (PAA, molecular weight: 450,000, Sigma-Aldrich, USA, CAS No. 9003-01-4, not a hazardous substance or mixture) or 1.5 g of poly (aspartic acid) (PASP, molecular weight: 6000–8000, Aike Reagent, China, CAS No. 25608-40-6, not a hazardous substance or mixture) was dissolved in 10 mL of deionized water to form a 0.3 g/mL PAA or a 0.15 g/mL PASP solution, respectively. 6 g of sodium hydroxide (NaOH, 97%, Aladdin,

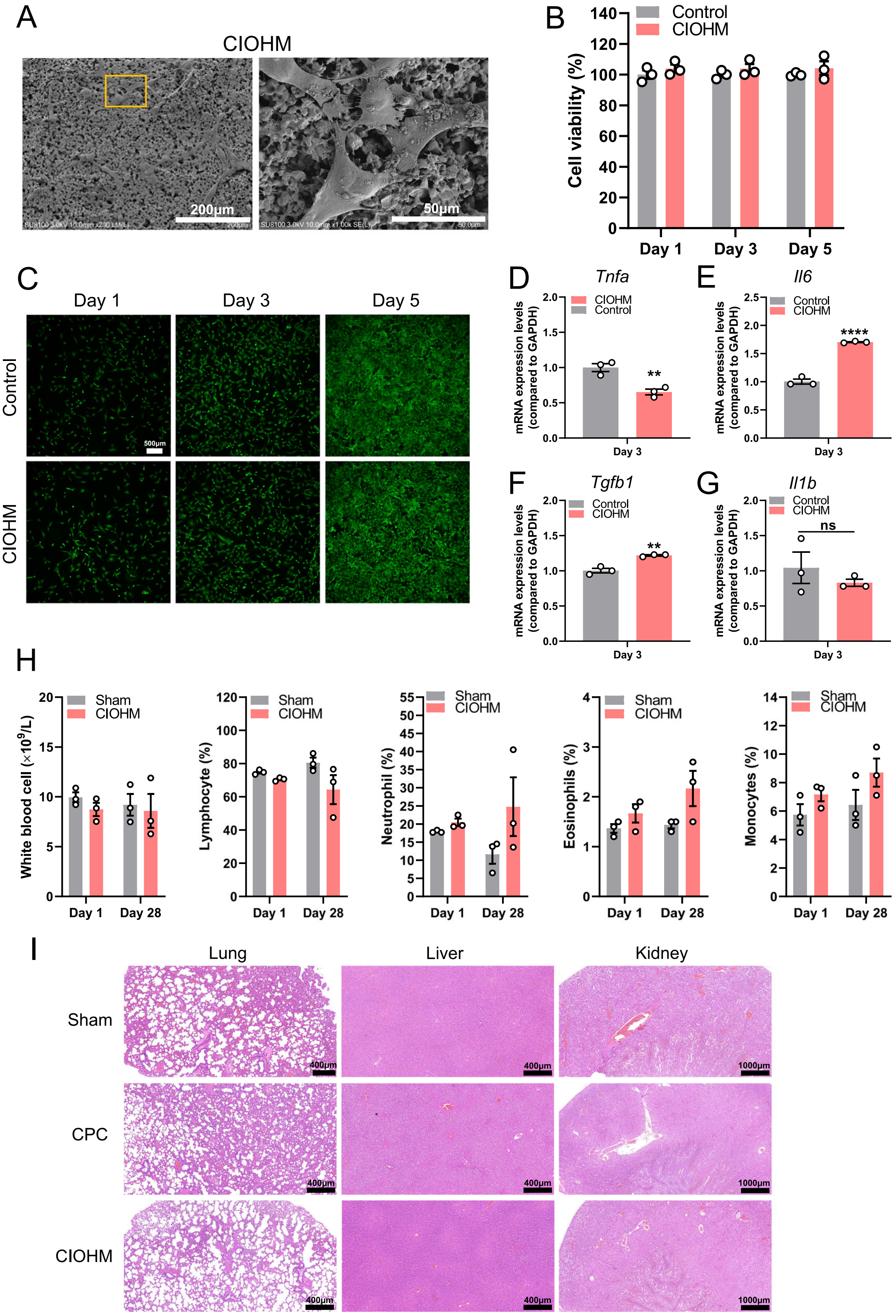

China, CAS No. 1310-73-2, causes skin burns and eye damage) was dissolved in 50 mL of deionized water to make a 3 M NaOH solution. A mixture was prepared by combining 2 mL of 0.1 M Na_2HPO_4, 0.4 mL of 0.3 g/mL PAA, and 0.15 g/mL PASP. CaP nanoclusters were obtained by dropwise adding this mixture into a prepared solution containing 0.1 M $CaCl_2$ and 0.2 mL of 0.3 g/mL PASP, followed by pH adjustment to 7.4 using a 3 M NaOH solution. After that, CaP nanoclusters were used as prepared without isolation or purification. The solution phase was completed by combining the CaP nanoclusters with incremental additions of citric acid (0.6% and 1.2%, wt%, 99.5%, Aladdin, China, CAS No. 77-92-9, causes serious eye irritation) and polyvinylpyrrolidone (PVP, 1.2% wt%, molecular weight: 10,000, Sigma-Aldrich, USA, CAS No. 9003-39-8, not a hazardous substance or mixture). The powder phase consisted of tetracalcium phosphate (TTCP, FUJIFILM Wako Pure

Fig. 5 | Biocompatibility assessment of CIOHMs. A Left panel: scanning electron microscopy (SEM) images depict human bone marrow mesenchymal stem cells (hBMMSCs) adhere to the surface of CIOHM and exhibit robust growth. Right panel: zoomed-in view of the yellow square area in the left panel. Scale bars represent 200 μm (left) and 50 μm (right). **B** CCK-8 assay of hBMMSCs cultured in extractions of CIOHM for 1 day, 3 days, and 5 days, respectively ($n = 3$ biological replicates). **C** Representative images of in vitro Live/Dead assay of hBMMSCs cultured in extractions of CIOHM for 1 day, 3 days, and 5 days, respectively. Green for live cells, red for dead cells. Scale bars represent 500 μm. **D**–**G** Inflammatory cytokine gene expressions of *Tnfa*, *Il6*, *Tgfb1,* and *Il1b* in RAW264.7, respectively ($n = 3$ technical replicates). Statistical significances were assessed by unpaired two-tailed Student's *t* tests. **: $P < 0.01$, ****: $P < 0.0001$, ns: no significant difference, *P*-Value = 0.0073 (**D**), *P*-Value < 0.0001 (**E**), *P*-Value = 0.0029 (**F**), *P*-Value = 0.4024 (**G**). **H** Peripheral blood immune cell counts after subcutaneous implantation of CIOHM in rats at 24 h and 28 days after implantation ($n = 3$ biological replicates). **I** Longitudinal in vivo assessment of CIOHM safety in a rat model at 8 weeks post-implantation. The histological analysis is visualized using hematoxylin and eosin (H&E) staining. Scale bars represent 400 μm (the lungs and liver) and 1000 μm (the kidneys), respectively. Data in (**B**) is presented as mean values +/− SD, whereas D-H are presented as mean values +/− SEM.

Chemical Corporation, Japan, CAS No. 1306-01-0, not a hazardous substance or mixture) and dicalcium phosphate anhydrous (DCPA, 97.5-102.5% anhydrous basis, Sigma-Aldrich, USA, CAS No. 7757-93-9, not a hazardous substance or mixture).

0.75 mL of the solution phase and 1 g of the powder phase were thoroughly mixed at a ratio of 0.75 mL/g to initiate the reaction. The resulting paste-like material was cast into molds and transferred to an incubator maintained at 37 °C with 50% relative humidity, where it was allowed to cure and set over a period of 24 h. The resultant was the CIOHM-GS. The CIOHM-HS was obtained by immersing CIOHM-GS in deionized water for 60 min.

Water absorption test

Water uptake was quantified through gravimetric analysis. CIOHM-GS were desiccated in an oven at 60 °C until a constant weight (W_O) was achieved. Subsequently, they were submerged in deionized water for predetermined intervals, with a total immersion time of 1 h. The samples were weighed every 2 min for the first 20 min, every 5 min for the following 20 min, and every 10 min for the last 20 min. Prior to each weighing, any unabsorbed water on the sample surfaces was removed using absorbent paper. The degree of water absorption was calculated using the formula: Water Absorption (%) = $((W_t - W_O) / W_O) \times 100\%$, where W_t represents the weight at time *t*.

Scanning electron microscopic analyses

For morphological characterizations, both of CIOHM-GS and CIOHM-HS were snap-frozen in liquid nitrogen and subsequently freeze-dried in a vacuum freeze-dryer (Model FD-1A-80, BIOCOOL, China) for 12 h to ensure complete ice sublimation. The dried samples were then sputter-coated with gold. Surface morphologies were observed using a Field Emission Scanning Electron Microscope (FE-SEM, FEI Quanta S-4800). Distributions of elements were analyzed using an Energy Dispersive Spectrometer (EDS).

To evaluate cell adhesion, human bone marrow mesenchymal stem cells (hBMMSCs) were seeded onto the CIOHM surfaces. The cells were cultured in 24-well plates using α-MEM (Minimal Essential Medium Alpha, Gibco, USA) supplemented with 10% fetal bovine serum (FBS, Gibco, USA) and an antibiotic mixture (100 μ/mL penicillin and 100 μg/mL streptomycin, Thermo Fisher Scientific, USA). Cultures were maintained at 37 °C in a 5% CO_2 atmosphere for 24 h. After incubation, the samples were fixed with 4% paraformaldehyde, rinsed three times with phosphate-buffered saline (PBS), and dehydrated in a graded alcohol series. The samples were then processed in a critical point dryer (Model K850, Quorum, UK), sputter-coated with gold, and observed under FE-SEM.

Compression tests

Cylindrical specimens (height: 12 mm; diameter: 6 mm) were prepared by casting pre-solidified CIOHM into customized molds and cured at 37 °C for 24 h. Compression tests of both CIOHM-GS and CIOHM-HS were performed using an Instron Universal Testing Machine (Model LEGEND 2344, USA) with a compressive force limit of 500 N and a loading speed of 10 mm/min. To investigate the influence of environmental conditions on mechanical behaviors, the compression tests were also conducted at 4 °C and 60 °C using CIOHM-HS. The elastic behavior was evaluated at incremental strains of 10, 20, 30, 40, and 50%. Compressive fatigue resistance was evaluated by subjecting CIOHM-HS to 1000 compression cycles at a maximum strain of 10%. For the long-term mechanical stability assessment, CIOHM-HS were incubated in sterile PBS at 37 °C for 70 days, with PBS refreshed every 3 days prior to the compression tests. A minimum of three specimens were tested for each condition.

Tensile tests

Customized molds were utilized to fabricate lamellar samples (1 mm × 8 mm × 40 mm) of CIOHM, which were similarly cured at 37 °C for 24 h. Tensile tests of CIOHM-HS were performed on the aforementioned Instron machine, applying a maximum force of 500 N and a loading speed of 50 mm/min. For fatigue tests, the specimens underwent 1000 cycles of cyclic stretching at a maximum strain of 10%. Each test was replicated with a minimum of four samples per group.

Rheological analysis

The rheological properties of pre-solidified CIOHMs with varying CA contents were evaluated using a rotating electromagnet rheometer (MCR 302, Anton Paar, Austria). After mixing the solution and powder phases for 30 s, the resulting mixture was placed between two parallel plates (diameter: 15 mm; gap: 1 mm). Time sweep tests were performed at a fixed frequency of 1 Hz to measure the storage modulus (G′) and loss modulus (G″).

Transmission electron microscopy

For transmission electron microscopy (TEM) analysis, samples were ground and sonicated in deionized water for 30 min to disperse. Droplets of the dispersion were deposited onto carbon-coated copper grids and examined using a Hitachi HT7700 TEM.

High-resolution transmission electron microscopy

HRTEM was employed for detailed microscopic morphological analysis. Samples were soaked in ethyl ethanol for 30 min, and droplets of the dispersion were placed onto carbon-coated copper grids. Analysis was conducted using a field emission analytical transmission electron microscope (2100 F, Japan). Elemental mapping was also performed to analyze the distribution of elements within the materials.

Attenuated total reflection Fourier transform infrared spectroscopy

Dried and finely powdered samples were mixed with potassium bromide (KBr) and pressed into thin, translucent pellets for spectroscopic analysis. ATR-FTIR spectra were acquired using a SHIMADZU system, scanning from 400 to 4000 cm^{-1}. Reference spectra were obtained using blank KBr discs. To investigate the long-term chemical stability, CIOHMs were incubated in PBS for predetermined time points (7, 14, 21, and 28 days) at 37 °C before the sample preparation.

X-ray photoelectron spectroscopy

The CIOHMs were lyophilized and ground into fine powders, which were then fixed on a stainless-steel holder using a stainless-steel

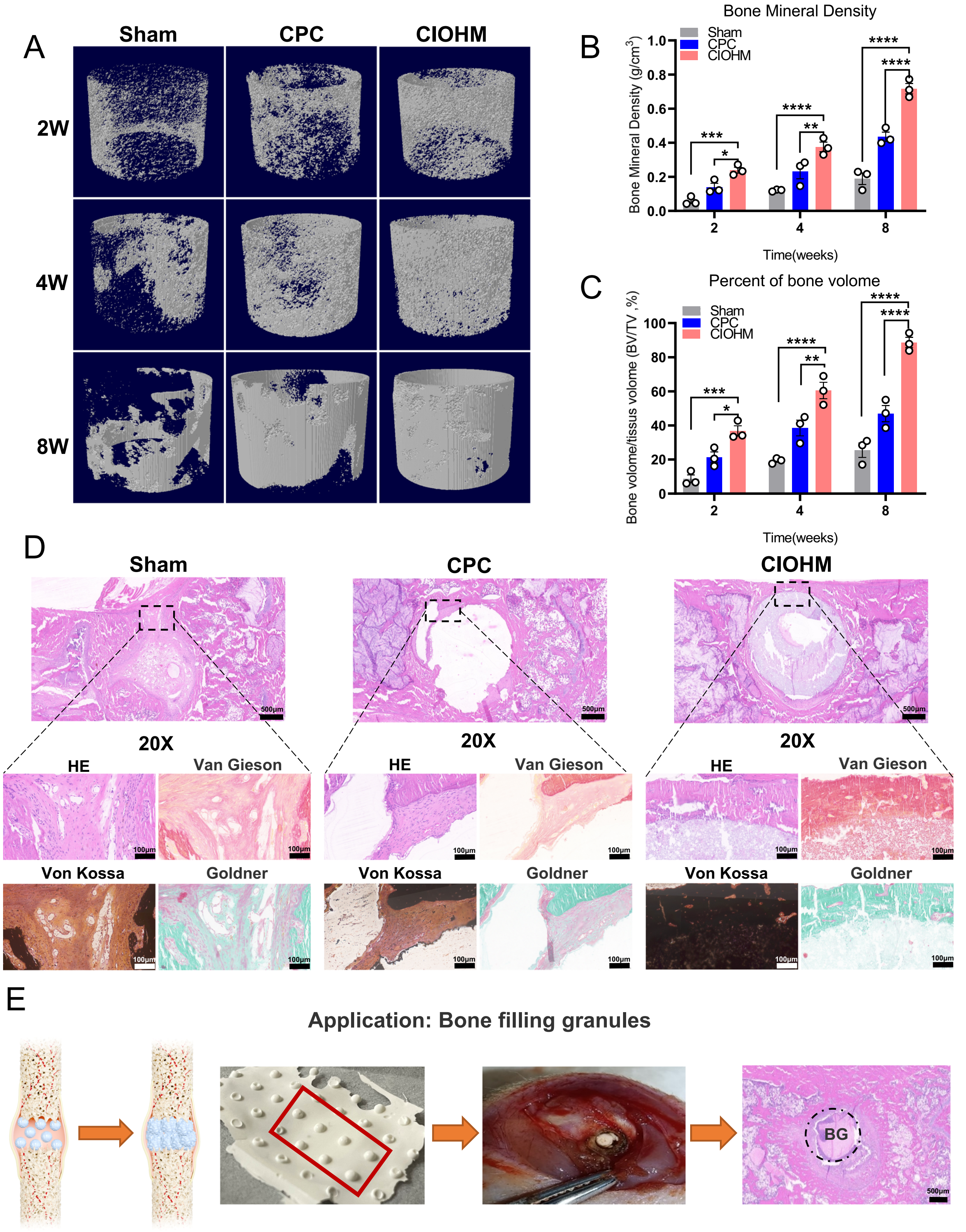

mask for the X-ray photoelectron spectroscopy (XPS) analyses. The XPS spectra were acquired by an ESCALAB system (VG ESCALAB MARK II, VG Scientific, United Kingdom) equipped with an Al K*α* source (1486.6 eV), operating at 300 W and an energy resolution of approximately 0.8 eV. The analyzer was positioned perpendicular to the sample surface.

X-ray diffraction

The crystalline compositions of CIOHMs were analyzed using X-ray diffraction (XRD, X'Pert PRO, PANALYTICAL, the Netherlands) with Cu Kα radiation ($\lambda = 1.54$ Å). The samples were ground into fine powders and exposed to CuKα radiation at 40 kV and 30 mA. Scans were performed at a step size of 10°/min over a 2θ range of 10–80°.

Fig. 6 | In vivo osteogenic effects and prospective clinical applications of the CIOHM. A Three-dimensional reconstructions illustrating new bone formation around implants at 2, 4, and 8 weeks post-implantation, derived from micro-CT data. B and C, Micro-CT-derived quantitative analyses of bone integration using sham surgery, calcium phosphate cement (CPC), and CIOHM implants show (**B**) bone mineral density (BMD) and (**C**) trabecular bone volume fraction (BV/TV) ($n = 3$ biological replicates). Data is presented as mean values +/- SEM. Statistical significance assessed by two-way ANOVA with Tukey's multiple comparisons test; $^*P < 0.05$, $^{**}P < 0.01$, $^{***}P < 0.001$, $^{****}P < 0.0001$; The *P*-Value (**B**): Sham vs. CPC = 0.1069 (2 weeks), 0.0237 (4 weeks), < 0.0001 (8 weeks), Sham vs. CIOHM = 0.0004 (2 weeks), < 0.0001 (4 weeks), < 0.0001 (4 weeks), CPC vs. CIOHM = 0.0435 (2 weeks), 0.0035 (4 weeks), <0.0001 (8 weeks); The *P*-Value (**C**): Sham vs. CPC = 0.0625 (2 week), 0.0044 (4 week), 0.0016 (8 week), Sham vs. CIOHM = 0.0001 (2 week), < 0.0001 (4 week), < 0.0001 (8 week), CPC vs. CIOHM = 0.0198 (2 week), 0.0013 (4 week), < .0001 (8 week); **D** Histological evaluations at 8 weeks post-implantation using H&E, Van Gieson's, von Kossa, and Goldner's trichrome staining methods to assess bone formation and integration in sham, CPC, and CIOHM groups. Representative sections are shown. Scale bars, 500 μm (overview) and 100 μm (detailed views). **E** Schematic representation of bone fracture treatment using bone filling granules made from CIOHM in rats' model, suggesting an alternative therapeutic approach for fracture healing.

To investigate the long-term chemical stability, CIOHMs were incubated in PBS for predetermined time points (7, 14, 21, and 28 days) at 37 °C before the sample preparation.

Thermogravimetric analysis/differential thermal analysis

Thermal behavior was evaluated using a thermogravimetric analysis/differential thermal analysis (TG/DTA) analyzer (SDT Q600, TA Instruments, USA). CIOHMs were heated from 25 °C to 800 °C at a rate of 10 °C/min under a nitrogen atmosphere. Both thermogravimetric (TG) and differential thermal analysis (DTA) curves were recorded to assess thermal stability and phase transformations.

Cell culture

The human bone marrow mesenchymal stem cells (hBMMSCs) were purchased from Cyagen Biosciences Inc. (HUXMA-01001, Guangzhou, China). The hBMMSCs were cultured using α-MEM (Gibco, USA) supplemented with 10% FBS (Gibco, USA) and an antibiotic mixture (100 μ/mL penicillin and 100 μg/mL streptomycin, Thermo Fisher Scientific, USA), in a CO_2 incubator (Forma Sterl-Cycle 371, Thermo Fisher Scientific, USA) at 37 °C with 5% CO_2. The murine-derived macrophage cell line RAW 264.7 cells were purchased from the National Collection of Authenticated Cell Cultures (SCSP-5036, Shanghai, China). The RAW 264.7 cells were cultured using Dulbecco's modified Eagle's medium (DMEM, Gibco) supplemented with 10% (v/v) FBS and antibiotics in a CO_2 incubator at 37 °C with 5% CO_2.

Extract solution preparation

According to the ISO 10993-1 standard[36], CIOHMs were sterilized in ethylene oxide, followed by incubation in the culture mediums at 0.2 g/mL in an incubator maintained at 37 °C and 5% CO_2. After 24 h, the samples were removed. The culture mediums were then centrifuged at 1097 × *g* for 10 min to separate any particulates, and the supernatants were filtered to ensure clarity and sterility for subsequent analyses.

Cell viability assay

hBMMSCs were seeded in 96-well plates at a density of 5000 cells per well and cultured in an incubator at 37 °C with 5% CO_2 for 24 h. The mediums were then replaced with the extract solutions. Cell viabilities were assessed at 1, 3, and 5 days using the Cell Counting Kit-8 (CCK-8, CK04, Dojindo, Japan) following the manufacturer's protocol. Briefly, the extract solutions were replaced with fresh culture mediums containing CCK-8 solution at a 10:1 ratio. After incubation for 1–2 h, the absorbance at 450 nm was measured using a microplate reader (Epoch, BioTek, USA).

Live/Dead assay

hBMMSCs were cultured in Dulbecco's Modified Eagle Medium (DMEM) supplemented with 10% fetal bovine serum (FBS) and 1% penicillin-streptomycin solution. The cells were incubated in a constant temperature CO_2 incubator. The materials were sterilized using ethylene oxide and then dispersed in PBS for 30 min. Subsequently, the materials were redispersed into DMEM at a concentration of 0.2 g/mL for 24 h in a 37 °C incubator. The incubation medium was then centrifuged at 1097 × *g* for 10 min, and the supernatant was used for cell-based experiments. The Live/Dead assay was performed at 1, 3, and 5 days using a live-dead cell staining kit (BioVision Inc., Milpitas, CA, USA) to assess hBMMSCs viability.

Hemolysis test

In vitro hemolysis tests were performed using rabbit blood. Whole blood was collected and mixed with sodium citrate anticoagulant at a ratio of 1:9. The experimental groups were as follows: CIOHM group, consisting of 1 mL of whole blood mixed with CIOHM; positive control group, with 0.5 mL distilled water (ddH_2O) and 0.5 mL whole blood; and negative control group, with 0.5 mL saline and 0.5 mL whole blood. The samples were incubated at 37 °C for 1 h. After incubation, samples were centrifuged at 1097 × *g* for 10 min, and the absorbance of the supernatant was measured at 450 nm using a microplate reader (Epoch, BioTek, USA). The hemolysis rate was calculated as: Hemolysis rate = (absorbance $_{\text{experimental group}}$ - absorbance $_{\text{negative control group}}$) / (absorbance $_{\text{positive control group}}$ - absorbance $_{\text{negative control group}}$)[37]. A hemolysis rate ≤5% indicates that the material does not exhibit hemolytic effects.

Coagulation test

Coagulation assays were performed using rabbit blood anticoagulated with sodium citrate (9:1 volume ratio). The blood was centrifuged at 1580 × *g* for 15 min at room temperature to isolate plasma. A 200 μL aliquot of plasma was added to the sample well of a coagulation analyzer plate (MC100, Pushkang, China), while 200 μL of deionized water was added to the corresponding blank well. Coagulation times were automatically determined using the coagulation analyzer.

Animal study

Animal experiments were approved by the Ethics Committee of the University of Hong Kong-Shenzhen Hospital ([2018]92). Sprague–Dawley (SD) rats were purchased from Zhuhai BesTest Bio-Tech Co., Ltd (Zhuhai, China). The effect of sex was not considered in this study, and rats of the same sex were used for the convenience of the experiment. A total of 18 3-month-old male SD rats were randomly divided into three groups ($n = 6$ per group): CPC group, CIOHM group, and Sham group. The administration of anesthesia was performed using an inhalation technique facilitated by a dedicated small animal anesthesia machine (Model TAIJI-IE, RWD, China). Isoflurane (Catalog R510-22-16, RWD, China) was chosen as an anesthetic agent. An initial induction concentration of 3% isoflurane was employed within a sealed anesthetic chamber until subjects demonstrated loss of righting reflex and lack of responsiveness. Subsequently, the rats were fitted with an anesthetic mask to maintain anesthesia at a reduced concentration of 2% isoflurane throughout the surgical procedure. The surgical site, specifically the right femoral distal epicondyle, was prepared by removal of fur and application of antiseptics. Using an electric drill (Model 78001, RWD, China). A standardized bone defect measuring 3 mm in diameter and 4 mm in depth was created. The defect was thoroughly irrigated with saline to ensure a clean environment before grafting. The CPC and CIOHM groups respectively received their corresponding material implants into the prepared bone cavity; the Sham group underwent the identical surgical procedure but without material implantation. Post-surgical care involved wound closure via layered suturing followed by topical antiseptic application. Animals were then returned to their housing facilities to recover under regular husbandry conditions.

The in vivo biocompatibility test was conducted in accordance with ISO 10993-11. A total of six 12-week-old male SD rats were randomly divided into two groups ($n = 3$ per group). The rats were anesthetized and shaved, and an incision was made along the midline of the back. CIOHM discs (12 mm diameter, 2 mm thickness) were implanted subcutaneously on the left side, while the Sham group underwent the same procedure without disc retention. Systemic toxicity observations were performed immediately post-implantation and at 4, 24, 48, and 72 h after surgery. The test samples were considered compliant if no adverse reaction in the experimental group exceeded those in the control animals. If two or more animals died or exhibited abnormal reactions, such as convulsions or collapse, or if three or more animals lost more than 10% of their body weight, the test samples were deemed non-compliant. At 24 h and 28 days postoperatively, orbital blood was collected for a Complete Blood Count (CBC) using an Automated Hematology Analyzer (BM830, Beijing Bowlinman Sunshine Science & Technology, China). Finally, the animals were euthanized, and their livers, kidneys, and lungs were excised, weighed, and photographed.

Preparation of hemispheric implants

To further elucidate our findings, hemispherical implants of both CPC and CIOHM, each with a diameter of 1.5 mm, were prepared and subsequently utilized as fillers for the artificially induced bone defects in 3-month-old male SD rats ($n = 6$).

Real-time micro-computed tomography (Micro-CT) analysis

At 2, 4, and 8 weeks post-surgery, rats were scanned using a micro-CT (Skyscan 1176, Bruker, Germany) with parameters set to 65 kVP energy, 385 μA intensity, 283 s scan time, 18.04 μm resolution, dual-frame averaging (bx2 mode), and 360° rotation at 0.5° increments. Three-dimensional reconstructions were generated using NRecon software, and morphometric parameters, including tissue volume (TV), bone volume (BV), BV/TV, bone mineral density (BMD), trabecular thickness (Tb.Th), trabecular number (Tb.N), and trabecular separation (Tb.Sp), were analyzed using CTAn software. An annular region (ROI) with a 12-pixel thickness surrounding the implant was selected for analysis. Calibration was performed using two standard rods (0.25 g/cm^3 and 0.75 g/cm^3), and grayscale thresholds of 80-255 were set for densitometric analysis.

Histological analysis

Bones were processed using hard tissue sectioning, whereas other organs were processed using soft tissue sectioning. The rats were euthanized at 4 and 8 weeks, and organs, including femurs, lungs, livers, and kidneys, were fixed in 4% paraformaldehyde for 48 h. Visceral organs were dehydrated through alcohol gradients and embedded in paraffin (EG1150 H, Leica, Germany), and sectioned at 4 μm using a microtome (RM2235, Leica, Germany). Sections were stained with hematoxylin and eosin (H&E) (G1004, Servicebio, China). Femurs were embedded in polymethyl methacrylate under vacuum for 5 h, and then polymerized in a 37 °C water bath, sectioned at 10 μm using a hard tissue microtome (HistoCore AUTOCUT, Leica, Germany) equipped with blades (TC-65, Leica, Germany). Sections were heated overnight at 60 °C, and stained with H&E, Von Kossa, Van Gieson, and Goldner's trichrome (G1043, G1046, G1064, Servicebio, China), respectively. Digital scanning of stained sections was performed with a digital slide scanner (Pannoramic MIDI, 3DHISTECH, Hungary).

Degradation rate analysis

Samples were freeze-dried using a vacuum freeze-dryer (Model FD-1A-80, BIOCOOL, China) for 24 h and weighed to determine the initial mass (M_O). The samples were then immersed in PBS at a ratio of 1 g per 20 mL solution and placed in an incubator at 37 °C, with the PBS being refreshed every 3 days. At days 3, 7, 14, 21, and 28, the samples were removed, freeze-dried for 24 h, and weighed (M_t). Four independent replicates were conducted for each time point. The percentage of remaining mass was calculated using the equation: $((M_O - M_t) / M_O \times 100\%)$. ATR-FTIR and XRD were also performed to investigate the chemical changes, using the same methods mentioned above.

Quantitative real-time PCR analyses

RAW 264.7 cells were seeded in 24-well plates at a density of 300,000 cells per well. After 12 h, the culture medium was replaced with CIOHM extracts, and the cells were cultured for 3 days. Total RNA was extracted using an RNAprep Pure Cell/Bacteria Kit (DP430, TIANGEN, China), and cDNA synthesis was performed using the RevertAid First Strand cDNA Synthesis Kit (K1622, Thermo Fisher Scientific, United States) on a Veriti™ DX 96-Well Thermal Cycler (Life Technologies, United States). Quantitative real-time PCR (qRT-PCR) was then conducted on the real-time PCR system (CFX Connect, Bio-Rad, United States) with QuantiNova™ SYBR Green PCR Master Mix (208054, Qiagen, Germany). Primer sequences for target genes are listed in Supplementary Table 1, with *Gapdh* serving as the housekeeping gene. Relative gene expression was calculated using the $2^{\hat{}-\Delta\Delta Ct}$ method. All test procedures followed the manufacturer's instructions. Three samples were tested in each group.

Statistical analysis

All experiments were performed at least three times. Results were presented as mean ± standard deviation (s.d.) or mean ± standard error of the mean (s.e.m.), along with the number of biological replicates or independent samples. GraphPad Prism v.8 (GraphPad Software, USA) and Origin Pro v.8.5 (OriginLab, USA) were employed for data analysis and graphical representation. Blender v.4.0 (Blender Foundation, the Netherlands) was utilized for three-dimensional simulations. Statistical significance was determined with unpaired two-tailed Student's *t* tests for two-group comparisons and one-way or two-way analysis of variance (ANOVA) for multiline comparisons, with P-values < 0.05 considered significant.

Reporting summary

Further information on research design is available in the Nature Portfolio Reporting Summary linked to this article.

Data availability

All relevant data that support the findings of this study are provided in the Source Data file. The full image dataset is available from the corresponding author upon request. Source data are provided in this paper.

References

1. Feng, C. et al. A novel hollow-tube-biphasic-whisker-modified calcium phosphate ceramics with simultaneously enhanced Mechanical Strength and Osteogenic Activity. *Adv. Funct. Mater.* **32**, 16 (2022).
2. Zhang, Y. G. et al. Biodegradable elastic sponge from nanofibrous biphasic calcium phosphate ceramic as an advanced material for regenerative medicine. *Adv. Funct. Mater.* **31**, 12 (2021).
3. Studart, A. R. BIOINSPIRED CERAMICS Turning brittleness into toughness. *Nat. Mater.* **13**, 433–435 (2014).

4. Meyers, M. A., Chen, P. Y., Lopez, M. I., Seki, Y. & Lin, A. Y. M. Biological materials: A materials science approach. *J. Mech. Behav. Biomed. Mater.* **4**, 626–657 (2011).
5. Bouville, F. et al. Strong, tough and stiff bioinspired ceramics from brittle constituents. *Nat. Mater.* **13**, 508–514 (2014).
6. Zhao, H. & Guo, L. Nacre-inspired structural composites: Performance-enhancement Strategy and perspective. *Adv. Mater.* **29**, https://doi.org/10.1002/adma.201702903 (2017).
7. Fang, W. et al. Organic–inorganic covalent–ionic molecules for elastic ceramic plastic. *Nature* **619**, 293–299 (2023).
8. Chen, T., Pauly, M. & Reis, P. M. A reprogrammable mechanical metamaterial with stable memory. *Nature* **589**, 386–390 (2021).
9. Zhao, H. et al. A hydrogel-based mechanical metamaterial for the interferometric profiling of extracellular vesicles in patient samples. *Nat. Biomed. Eng.* **7**, 135–148 (2023).
10. Sharma, A. et al. Inorganic/organic combination: Inorganic particles/polymer composites for tissue engineering applications. *Bioact. Mater.* **24**, 535–550 (2023).
11. Davami, K. et al. Ultralight shape-recovering plate mechanical metamaterials. *Nat. Commun.* **6**, 7 (2015).
12. Ye, M. L., Gao, L. & Li, H. A design framework for gradually stiffer mechanical metamaterial induced by negative Poisson's ratio property. *Mater. Des.* **192**, 15 (2020).
13. Liu, K. et al. 4D printed zero Poisson's ratio metamaterial with switching function of mechanical and vibration isolation performance. *Mater. Des.* **196**, 10 (2020).
14. Chen, B. C. et al. Novel multifunctional negative stiffness mechanical metamaterial structure: Tailored functions of multi-stable and compressive mono-stable. *Compos. B Eng.* **204**, 16 (2021).
15. Morris, C., Bekker, L., Spadaccini, C., Haberman, M. & Seepersad, C. Tunable mechanical metamaterial with constrained negative stiffness for improved quasi-static and dynamic energy dissipation. *Adv. Eng. Mater.* **21**, 8 (2019).
16. Jiang, Y. Y. & Li, Y. N. Novel 3D-printed hybrid auxetic mechanical metamaterial with chirality-induced sequential Cell Opening Mechanisms. *Adv. Eng. Mater.* **20**, 9 (2018).
17. Zhang, X. Y., Ren, X., Zhang, Y. & Xie, Y. M. A novel auxetic metamaterial with enhanced mechanical properties and tunable auxeticity. *Thin Walled Struct.* **174**, 13 (2022).
18. Yao, S. et al. Calcium phosphate nanocluster-loaded injectable hydrogel for bone regeneration. *ACS Appl. Bio Mater.* **2**, 4408–4417 (2019).
19. Weng, L. H., Chen, X. M. & Chen, W. L. Rheological characterization of in situ crosslinkable hydrogels formulated from oxidized dextran and N-carboxyethyl chitosan. *Biomacromolecules* **8**, 1109–1115 (2007).
20. Rhee, S. H. & Tanaka, J. Hydroxyapatite coating on a collagen membrane by a biomimetic method. *J. Am. Ceram. Soc.* **81**, 3029–3031 (1998).
21. Yokoyama, A., Yamamoto, S., Kawasaki, T., Kohgo, T. & Nakasu, M. Development of calcium phosphate cement using chitosan and citric acid for bone substitute materials. *Biomaterials* **23**, 1091–1101 (2002).
22. Nie, Y. P. et al. Characterization of a high strength hydroxyapatite cement with dual chelate-setting using phytic acid and citric acid. *Int. J. Appl. Ceram. Technol.* **19**, 1498–1510 (2022).
23. Wang, S. et al. Citric acid enhances the physical properties, cytocompatibility and osteogenesis of magnesium calcium phosphate cement. *J. Mech. Behav. Biomed. Mater.* **94**, 42–50 (2019).
24. Diani, J., Fayolle, B. & Gilormini, P. A review on the Mullins effect. *Eur. Polym. J.* **45**, 601–612 (2009).
25. Liu, N. et al. Calcium phosphate cement with icariin-loaded gelatin microspheres as a local drug delivery system for bone regeneration. *BioMed. Eng. OnLine* **21**, https://doi.org/10.1186/s12938-022-01052-0 (2022).
26. Vladescu, A. et al. Mechanical properties and biocompatibility of the sputtered Ti doped hydroxyapatite. *J. Mech. Behav. Biomed. Mater.* **63**, 314–325 (2016).
27. Negrila, C., Predoi, M., Iconaru, S. & Predoi, D. Development of zinc-doped hydroxyapatite by sol-gel method for medical applications. *Molecules* **23**, https://doi.org/10.3390/molecules23112986 (2018).
28. Ji, J., Joh, H. I., Chung, Y. & Kwon, Y. Glucose oxidase and polyacrylic acid based water swellable enzyme-polymer conjugates for promoting glucose detection. *Nanoscale* **9**, 15998–16004 (2017).
29. Li, D. S. et al. Evaluation of biocompatibility and immunogenicity of micro/nanofiber materials based on tilapia skin collagen. *J. Biomater. Appl.* **33**, 1118–1127 (2019).
30. Yang, J. et al. Effect of chitosan molecular weight and deacetylation degree on Hemostasis. *J. Biomed. Mater. Res. Part B* **84B**, 131–137 (2008).
31. Guo, X. et al. Effects of chitosan oligosaccharides on human blood components. *Front. Pharmacol.* **9**, 10 (2018).
32. Winge, M. I. & Røkkum, M. Calcium phosphate bone cement and metaphyseal -corrective osteotomies in the upper extremity: long-term follow-up of 10 children. *Acta Orthop.* **93**, 769–774 (2022).
33. Feroze, R. A., Agarwal, N. & Sekula, R. F. Utility of calcium phosphate cement cranioplasty following supraorbital approach for tumor resection. *Int. J. Neurosci.* **128**, 1199–1203 (2018).
34. Higuchi, T. et al. Calcium phosphate Cement in the surgical management of benign bone tumors. *Anticancer Res.* **38**, 3031–3035 (2018).
35. Vezenkova, A. & Locs, J. Sudoku of porous, injectable calcium phosphate cements - Path to osteoinductivity. *Bioact. Mater.* **17**, 109–124 (2022).
36. Li, P. et al. Selection of extraction medium influences cytotoxicity of zinc and its alloys. *Acta Biomater.* **98**, 235–245 (2019).
37. Tong, X. et al. Degradation behavior, cytotoxicity, hemolysis, and antibacterial properties of electro-deposited Zn-Cu metal foams as potential biodegradable bone implants. *Acta Biomater.* **102**, 481–492 (2020).

Acknowledgements

We thank Dr. Ziyang Xu of Tianjin University for his solid support in the mechanical tests. We thank Dr. Wangyong Zhu of the University of Hong Kong-Shenzhen Hospital for his clinical guidance on mandibular prosthesis. We thank Dr. Danni Shen of Zhejiang University for her solid support of micro-CT analysis. This work was financially supported by the National Key R&D Program of China (2023YFB3810200, K.W.K.Y.), Shenzhen Science and Technology Funding (JCYJ20220530142206014, J.W., JCYJ20210324120009026, K.W.K.Y., JCYJ20230807113016033, D.Z., & JCYJ20200109150420892, T.M.W.), Hong Kong Health and Medical Research Fund (nos. 22210832, 23220952 and 23220752, K.W.K.Y.).

Author contributions

F.L., R.T., K.W.K.Y., and J.W. conceived the idea. F.L., S.Y., and J.W. designed the experiments. F.L. performed the experiments. S.Y. performed the microstructural and compositional analysis. J.L. performed the chemical structure analysis. K.H. performed the cytotoxicity test and synthesis of CaP nanoclusters. F.L., D.Z., and T.M.W. performed the animal experiment. F.L., S.Y., and J.W. wrote the manuscript with input from all authors. All authors analyzed and discussed the results and commented on the manuscript. R.T., K.W.K.Y., and J.W. provided funding and supervised the study.

Competing interests

The authors declare no competing interests.

Additional information

Supplementary information The online version contains supplementary material available at https://doi.org/10.1038/s41467-025-59662-w.

Correspondence and requests for materials should be addressed to Ruikang Tang, Kelvin W. K. Yeung or Jun Wu.

Peer review information *Nature Communications* thanks the anonymous reviewer(s) for their contribution to the peer review of this work. A peer review file is available.

Reprints and permissions information is available at http://www.nature.com/reprints

Publisher's note Springer Nature remains neutral with regard to jurisdictional claims in published maps and institutional affiliations.

Open Access This article is licensed under a Creative Commons Attribution-NonCommercial-NoDerivatives 4.0 International License, which permits any non-commercial use, sharing, distribution and reproduction in any medium or format, as long as you give appropriate credit to the original author(s) and the source, provide a link to the Creative Commons licence, and indicate if you modified the licensed material. You do not have permission under this licence to share adapted material derived from this article or parts of it. The images or other third party material in this article are included in the article's Creative Commons licence, unless indicated otherwise in a credit line to the material. If material is not included in the article's Creative Commons licence and your intended use is not permitted by statutory regulation or exceeds the permitted use, you will need to obtain permission directly from the copyright holder. To view a copy of this licence, visit http://creativecommons.org/licenses/by-nc-nd/4.0/.

© The Author(s) 2025